

H.E.S.S. follow-up observations of GRB 221009A

H.E.S.S. COLLABORATION

Submitted to ApJL

ABSTRACT

GRB 221009A is the brightest gamma-ray burst ever detected. To probe the very-high-energy (VHE, >100 GeV) emission, the High Energy Stereoscopic System (H.E.S.S.) began observations 53 hours after the triggering event, when the brightness of the moonlight no longer precluded observations. We derive differential and integral upper limits using H.E.S.S. data from the third, fourth, and ninth nights after the initial GRB detection, after applying atmospheric corrections. The combined observations yield an integral energy flux upper limit of $\Phi_{\text{UL}}^{95\%} = 9.7 \times 10^{-12} \text{ erg cm}^{-2} \text{ s}^{-1}$ above $E_{\text{thr}} = 650 \text{ GeV}$. The constraints derived from the H.E.S.S. observations complement the available multiwavelength data. The radio to X-ray data are consistent with synchrotron emission from a single electron population, with the peak in the SED occurring above the X-ray band. Compared to the VHE-bright GRB 190829A, the upper limits for GRB 221009A imply a smaller gamma-ray to X-ray flux ratio in the afterglow. Even in the absence of a detection, the H.E.S.S. upper limits thus contribute to the multiwavelength picture of GRB 221009A, effectively ruling out an IC dominated scenario.

Keywords: Gamma-rays: general, Gamma-rays: bursts, emission mechanism: non-thermal

1. INTRODUCTION

In the last few years, several gamma-ray bursts (GRBs) have been detected in Very-High-Energy (VHE, >100 GeV) gamma rays (Abdalla et al. (H.E.S.S. Collaboration) 2019; MAGIC Collaboration et al. 2019; Abdalla et al. (H.E.S.S. Collaboration) 2021). These explosive phenomena originate from the deaths of massive stars or the mergers of compact objects (e.g. Mészáros 2002). GRBs are observed as bright flashes of gamma rays, referred to as the prompt emission, followed by long-lived and slowly evolving multiwavelength afterglow emission (see Noda & Parsons (2022) for a recent review of VHE observations of GRBs). The prompt emission is thought to come from interactions within the ultrarelativistic jet produced by the catastrophic progenitor event, though the development of accurate theoretical models of the physical mechanisms underlying the emission are challenging (Iyyani 2022). In contrast,

the afterglow is produced by the jet’s subsequent interactions with the surrounding environment, and during this time the jet is well described as a conical section of a decelerating spherical blast wave (see Dai et al. 2017, for a recent review of GRB theory). The GRB afterglow therefore provides a well-defined laboratory for studying particle acceleration under extreme conditions.

The primary emission mechanism of photons with energies $\ll \text{GeV}$ in the afterglow is well established as synchrotron emission by a population of accelerated charged particles. Assuming a homogeneous magnetic field, synchrotron photons can in principle extend up to a maximum energy $\approx 100\Gamma \text{ MeV}$, where Γ is the bulk Lorentz factor of the emission zone (de Jager et al. 1996; Abdalla et al. (H.E.S.S. Collaboration) 2021). A second spectral component associated with inverse Compton scattering of either ambient or the synchrotron photons is expected at higher energies, though tension between observations and single-zone synchrotron self-Compton (SSC) models have been found in the VHE domain (Abdalla et al. (H.E.S.S. Collaboration) 2021). The properties of any detected VHE emission therefore has important ramifications for GRB studies; the unambiguous detection of an SSC component would set constraints on the phys-

Corresponding author: J. Damascene Mbarubucyeye, H. Ashkar, S. J. Zhu, B. Reville, F. Schüssler
contact.hess@hess-experiment.eu

ical properties of the emission zone, while strong deviations from the expected SSC spectrum could indicate the need for a more complex set of assumptions. The two VHE-bright GRBs with the most complete data sets so far have not provided a firm conclusion on this issue (MAGIC Collaboration et al. 2019; Abdalla et al. (H.E.S.S. Collaboration) 2021).

The recent GRB 221009A is the GRB with the brightest detected prompt emission, and its redshift of $z = 0.151$ — corresponding to a luminosity distance of around 750 Mpc — implies an isotropic equivalent energy release in the prompt emission E_{iso} of the order of 10^{54} erg (de Ugarte Postigo et al. 2022), marking it as an extremely energetic GRB. The large E_{iso} and close proximity resulted in the potential detection for the first time of a GRB at energies above 10 TeV and likely the very first detection of VHE photons during the prompt phase, by the Large High Altitude Air Shower Observatory (LHAASO) (Huang et al. 2022a). To further extend this picture and characterize the VHE emission in the afterglow, the High Energy Stereoscopic System (H.E.S.S.) observed GRB 221009A on the third night, as soon as it became possible following a period of bright moonlight. H.E.S.S. is sensitive to photons at energies above tens of GeV, and has so far detected VHE emission from two GRBs (Abdalla et al. (H.E.S.S. Collaboration) 2019, 2021), including a detection more than 50 hours after the initial detection for GRB 190829A.

In this paper, we present the H.E.S.S. observations of GRB 221009A starting on the third night after the GRB detection. We discuss the observations themselves in Section 2, and the analysis of both H.E.S.S. data and multiwavelength data in Section 3. We find no significant emission from a source at the GRB position, and derive upper limits assuming an intrinsic E^{-2} spectrum. In order to place these into context, we discuss the multiwavelength modeling in Section 4, and conclude in Section 5. Throughout the paper we assume a flat Λ CDM cosmology with $H_0 = 67.4 \text{ km s}^{-1} \text{ Mpc}^{-1}$ and $\Omega_m = 0.315$ (Planck Collaboration et al. 2020).

2. OBSERVATIONS

2.1. Initial detection

The detection of the prompt emission of GRB 221009A was first reported by the *Fermi* Gamma-Ray Burst Monitor (GBM), which triggered on the GRB on 2022-10-09 at 13:16:59 UTC (Veres et al. 2022); we refer to the GBM trigger time as T_0 . GeV emission was also reported by the *Fermi* Large Area Telescope (LAT) (Bissaldi et al. 2022). The GRB also triggered the Neil Gehrels *Swift* Observatory once it became visible to the *Swift* Burst Alert Telescope an hour later. This caused

the satellite to automatically slew to the source, allowing for follow-up observations by the other instruments on *Swift* such as the X-Ray Telescope (XRT), which reported a localization of right ascension = 19h 13m 03s, declination = +19° 48' 09" (J2000) with a positional uncertainty of 5.6" (Dichiara et al. 2022).

2.2. H.E.S.S. observations

H.E.S.S. is a system of five Imaging Atmospheric Telescopes located in the Khomas Highland of Namibia (23°16'18", 16°30'00") at 1800m above sea level. Four 12-m telescopes (CT1-4) (Aharonian et al. (H.E.S.S. collaboration) 2006), each with a mirror area of 108 m², are placed in a square formation with 120m side. A fifth, 28-m telescope (CT5) with a mirror area of 612 m² is placed in the center of the array (Holler et al. 2015).

On October 9 and 10, H.E.S.S. could not observe the GRB as the night-sky background was too high due to the full Moon. On October 11, H.E.S.S. started observations with its 12-m telescopes as soon as observing conditions allowed. During that night, an extended 32-minute observation run was taken in nominal conditions during dark time (when the Moon was still below the horizon) followed by a second run using settings optimised for observations under high levels of optical background light such as moonlight (Tomankova et al. 2022). H.E.S.S. continued observing GRB 221009A in the following nights. The observations were conducted under poor atmospheric conditions due to clouds and a higher aerosol content in the atmosphere due to the regular biomass-burning season (Formenti et al. 2019). The quality of the atmospheric conditions is quantified by the atmospheric transparency coefficient (Hahn et al. 2014) with lower values corresponding to lower transmission of Cherenkov light through the atmosphere (Table 1). Nominally accepted values of the atmospheric transparency coefficient are above 0.8. As the transparency coefficients were lower than this during the H.E.S.S. observations of this GRB, a correction procedure has been applied (discussed in the next section). Additional datasets, including ones taken on other nights, are excluded from the analysis due to further degradation of the atmospheric conditions by the presence of clouds. Unfortunately, CT5 data are not available for this study. The data taken with CT1-4 are used. Table 1 summarizes the H.E.S.S. observations used in this analysis.

3. ANALYSIS AND RESULTS

3.1. H.E.S.S. analysis

The H.E.S.S. data acquired during the follow-up period are analyzed using the ImPACT reconstruction procedure (Parsons & Hinton 2014) which uses an image-

Calendar date	Interval	$T_{\text{Start}} - T_0$ [s]	$T_{\text{End}} - T_0$ [s]	Average zenith angle [deg]	ATC
October 11 2022	Night 3	1.901×10^5	1.920×10^5	49.3	0.46
October 11 2022 ^a	Night 3	1.922×10^5	1.929×10^5	52.7	0.44
October 12 2022	Night 4	2.765×10^5	2.782×10^5	49.6	0.49
October 12 2022	Night 4	2.783×10^5	2.800×10^5	52.6	0.45
October 12 2022	Night 4	2.800×10^5	2.818×10^5	57.0	0.41
October 17 2022	Night 9	7.087×10^5	7.104×10^5	51.7	0.47
October 17 2022	Night 9	7.105×10^5	7.122×10^5	56.9	0.65

^a taken under moderate moonlight

Table 1. H.E.S.S. observations of GRB 221009A. Column 2 denotes the number of nights after T_0 . Columns 3 and 4 represent the run start and end time since T_0 , in seconds, respectively. Column 5 shows the average zenith angle under which the observations were conducted and column 6 shows the Atmospheric Transparency Coefficient (ATC).

template-based maximum likelihood fit. The hadronic background events produced by cosmic rays are rejected with a multivariate analysis scheme (Ohm et al. 2009). The results are independently cross-checked with a separate analysis chain based on the Model Analysis (de Naurois & Rolland 2009) which performs a log-likelihood comparison between the recorded shower images and semianalytically generated templates. Moreover, in order to correct for atmospheric disturbances, we apply a scheme developed to assess the impact of the enhanced aerosol levels in the atmosphere on the instrument response functions derived from Monte-Carlo simulations. The scheme calculates a correction factor to the expected Cherenkov light by comparing the actual transmission profile with the ideal one used in the simulations. The correction is then applied by modifying *a posteriori* the instrument response functions and reconstructed event energies (Holch et al. 2022). These corrections are cross-checked by an analysis that uses dedicated *runwise* simulations taking into consideration the actual observation conditions and telescope configuration during the GRB 221009A H.E.S.S. observations following the method outlined in Holler et al. (2020). We use *loose cuts* (Aharonian et al. (H.E.S.S. collaboration) 2006) for the selection of gamma-ray showers. In the high-level analysis, we converted our data into GADF format¹ (Deil et al. 2022), and use the open source analysis package GAMMAPY (Deil et al. 2017; Acero et al. 2022) (v1.0).

In order to search for a possible signal, and avoid accidentally including emission from other sources, we generate maps of excess gamma-ray counts and significances within a range of +/- 2.0 degrees from the expected emission position. These maps are generated using the ring background technique (Berge et al. 2007) with cir-

cular ON regions of 0.122 deg centered at each point on the map, and corresponding annular OFF-source regions centered on the same positions with radii 0.5 to 0.8 deg to measure pure background. We exclude a circular region of 0.3 deg around the expected emission region from the OFF-source regions. When computing the exposure ratio between the ON and OFF-source region at each test position, a radially-symmetric model for the background acceptance within the field of view of each observation was integrated spatially over the regions. For all three nights combined, we obtain on the position of the source $N_{\text{ON}} = 39$ events and $N_{\text{OFF}} = 686$ events, with a ratio of on-source exposure to off-source exposure of 0.0638. Using the statistical formulation described in Li & Ma (1983) we calculate the excess counts to be -4.8 and we find N_{ON} events to be in agreement with the expected background at -0.7σ level. The excess and significance maps are derived and shown in Figure 1.

Following this analysis, we detect no significant emission of VHE gamma rays at the GRB location in the combined dataset nor for each night separately. We thus compute upper limits to constrain the VHE gamma-ray emission from the GRB at the time of H.E.S.S. observations using the Reflected Background method described in Berge et al. (2007) with same-size circular ON and OFF regions. The energy threshold E_{thr} sets the lower limit of the spectral analysis and is defined as the lowest energy at which the bias between reconstructed and simulated energies is below 10%. We find a value of $E_{\text{thr}} = 650$ GeV for the dataset combining all observations. We assume a generic intrinsic E^{-2} dN/dE spectrum, and use the redshift of the source $z = 0.151$ and the model of the extragalactic background light described in Domínguez et al. (2011), and compute 95% confidence level (C.L.) flux upper limits using a Poisson likelihood method described in Rolke et al. (2005). The

¹ <https://gamma-astro-data-formats.readthedocs.io/en/latest/index.html>

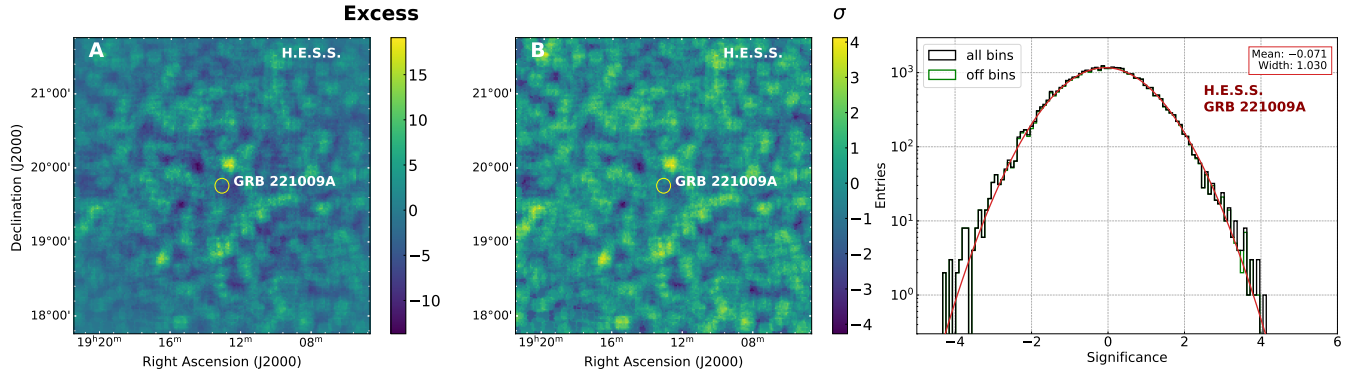


Figure 1. Left: Excess count map computed from the H.E.S.S. observational data taken on GRB 221009A presented in Table 1 with a 0.1° oversampling radius (yellow circle). Middle: Significance map computed from the H.E.S.S. excess count map of GRB 221009A. Right: Significance distribution of the H.E.S.S. significance map entries in black and a Gaussian distribution fit in red.

differential upper limits are shown in Figure 2. Detailed results are available on a dedicated webpage².

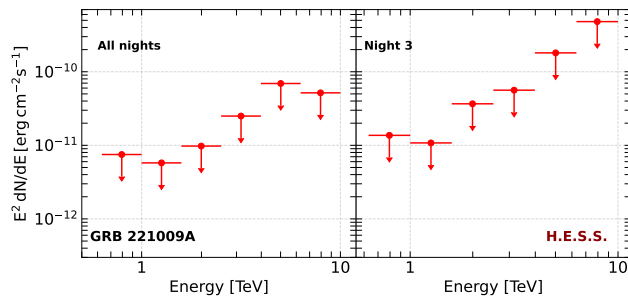


Figure 2. 95% C.L. differential flux upper limits on an intrinsic (EBL-corrected) E^{-2} GRB spectrum, derived from the H.E.S.S. observational data taken on GRB 221009A in all nights combined (left) and Night 3 only (right).

We compute integral flux upper limits between E_{thr} and 10 TeV for each night, where the upper bound is chosen to be the energy above which $N_{\text{OFF}} < 10$. The upper limits of the integral energy flux are shown in Figure 3. The combined dataset yields an integral energy flux upper limit of $\Phi_{\text{UL}}^{95\%} = 9.7 \times 10^{-12}$ erg cm⁻² s⁻¹, and per-night integral energy flux upper limits are given in Table 2. Systematic effects include uncertainties of the atmospheric corrections, the assumed intrinsic energy spectrum, differences in EBL absorption models and general uncertainties in the flux and energy scale. The systematic uncertainties are conservatively estimated to be about a factor of 2, with expected worsening of sys-

tematics with energy, for both the differential and integral upper limits on the gamma-ray flux.

3.2. Swift-XRT analysis

Swift-XRT is an X-ray imaging spectrometer with an energy range of 0.3 to 10 keV (Burrows et al. 2005). The XRT data are obtained using the Time-Sliced Spectra tool³ (Evans et al. 2009). The time intervals are chosen to overlap with the H.E.S.S. observations. There are no simultaneous XRT observations on two of the three H.E.S.S. nights, so we instead define the time ranges in such a way that they encompass one set of contiguous XRT observations immediately before and after the H.E.S.S. observations. However, using this rule for the first night of H.E.S.S. observations resulted in a too-low XRT exposure time. Hence, for this night we extend the time range to include *two* sets of contiguous XRT observations on either side. (Note that, as we are using larger time bins for the XRT observations, we are underestimating what the true uncertainties would be for strictly contemporaneous observations.) In our analyses, we only include Photon Counting (PC) data. By using the data products from the Time-Sliced Spectra tool and selecting only the PC mode data, we avoid contamination from the dust rings (Tiengo et al. 2022; Evans 2022).

The XRT data are fit using XSPEC v12.13.0c with a power law of the form $dN/dE = k(E/E_0)^{-\alpha}$ ($E_0 = 1$ keV) and two absorption components (Evans et al. 2009). More specifically, we fit the data with the model TBabs * zTBabs * powerlaw with the Galactic column density $N_{\text{H,gal}} = 5.38 \times 10^{21}$ cm⁻² (Willingale et al. 2013). We simultaneously fit the three nights with the

² https://www.mpi-hd.mpg.de/hfm/HESS/pages/publications/auxiliary/2023_GRB_221009A

³ https://www.swift.ac.uk/xrt_spectra/addspec.php?target=01126853&origin=GRB

Interval	Time since T_0 [s]	α	$k \times 10^{-2}$ [ph keV $^{-1}$ cm $^{-2}$ s $^{-1}$]	XRT en. flux $\times 10^{-11}$ [erg cm $^{-2}$ s $^{-1}$]	H.E.S.S. en. flux UL $\times 10^{-11}$ [erg cm $^{-2}$ s $^{-1}$]
Night 3	$(1.68 - 2.22) \times 10^5$	1.69 ± 0.10	2.14 ± 0.30	14.9 ± 2.3	4.06
Night 4	$(2.61 - 2.90) \times 10^5$	1.90 ± 0.12	1.31 ± 0.20	7.80 ± 1.33	1.77
Night 9	$(6.85 - 7.25) \times 10^5$	1.85 ± 0.25	0.23 ± 0.09	1.42 ± 0.62	2.85

Table 2. Results of analyses of XRT and H.E.S.S. data. The entries in the first column correspond to the second column of Table 1. The second through fourth columns show the results of fitting XRT data in time intervals bracketing the nights during which H.E.S.S. observed the GRB, with 1σ uncertainties (statistical only). The last column lists the H.E.S.S. energy flux upper limits for the time interval defined by the third and fourth columns of Table 1. The XRT energy flux is calculated in the 0.3–10 keV range and the H.E.S.S. energy flux in the 0.65–10 TeV range.

column density at the source $N_{\text{H,int}}$ tied across all spectra but free to vary, under the assumption that the intrinsic absorption does not vary on these timescales. We keep k and α free in each time interval. We define the fitting statistic to be the **C-statistic**⁴, suitable for XRT data. Assuming a constant $N_{\text{H,int}}$, we obtain $N_{\text{H,int}} = (1.32 \pm 0.18) \times 10^{22}$ cm $^{-2}$. The results are presented in Table 2 and plotted in Figure 3, and are compatible with those presented in Williams et al. (2023), which similarly reports a softening in the X-ray spectrum on these timescales.

The assumption of constant column density on these timescales has been challenged in other GRBs, recently by Campana et al. (2021) for GRB 190114C. For GRB 221009A, indications of a higher degree of absorption at earlier times have indeed been noted in the optical data (Fulton et al. 2023). Because there is some degeneracy between the effects of $N_{\text{H,int}}$ and α (e.g., a larger value of $N_{\text{H,int}}$ can be somewhat compensated by a softer value of α) this also has an effect on the returned best-fit photon spectrum. If $N_{\text{H,int}}$ is indeed higher around Night 3 (≈ 2 days after T_0) than the later nights, then the true value of α for Night 3 should be softer than the returned 1.7 and therefore more similar to the value of 1.9 that we find for the other two H.E.S.S. nights (although we note that the indices are consistent within 2σ). A thorough study of this effect is beyond the scope of this paper, so for the purposes of the discussion in Section 4, we do not require that our modeling explain the XRT data on Night 3 very strictly.

3.3. *Fermi-LAT* analysis

The *Fermi-LAT* is a pair conversion telescope that detects gamma rays between tens of MeV and hundreds of GeV (Atwood et al. 2009). We perform an unbinned likelihood analysis of *Fermi-LAT* data over time ranges spanning each set of H.E.S.S. observations (Table 1) us-

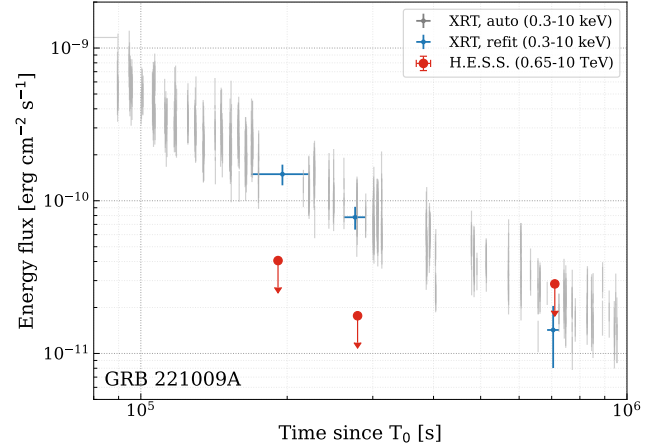


Figure 3. The H.E.S.S. integral energy flux upper limits (red circles; 95% C.L.) are derived assuming an intrinsic E^{-2} spectrum. The automated XRT data (gray) are obtained from the Burst Analyser^a (Evans et al. 2010); multiple XRT observations around the H.E.S.S. observations are then combined and refit (blue, 1σ uncertainty). Note that the Burst Analyser assumes a larger value of intrinsic absorption than we find in our analysis and therefore returns a larger unabsorbed energy flux. The extension of the H.E.S.S. error bars in the x direction, depicting the duration of the H.E.S.S. observations, is smaller than the size of the markers.

^a https://www.swift.ac.uk/burst_analyser/01126853/

^b https://www.swift.ac.uk/burst_analyser/01126853/

ing *gtBurst* v. 03-00-00p5 (Vianello 2016). We use the **P8R3_SOURCE** event class, recommended for analyses on these timescales, and the corresponding instrument response functions⁵. We select events in the energy range 100 MeV and 10 GeV within 12° of the burst position and a zenith angle cut of 100° . We use the **PowerLaw2** model⁶ for the GRB spectrum, and the latest Galactic (fixed normalization) and isotropic templates for the

⁵ https://fermi.gsfc.nasa.gov/ssc/data/analysis/documentation/Cicerone/Cicerone_LAT_IRFs/IRF_overview.html

⁶ https://fermi.gsfc.nasa.gov/ssc/data/analysis/scitools/source_models.html

⁴ <https://heasarc.gsfc.nasa.gov/xanadu/xspec/manual/XSappendixStatistics.html>

background⁷, and include all catalog sources (Abdollahi et al. 2020) within 20° of the GRB position. No significant emission from the GRB (Test Statistics < 1) is observed in the *Fermi*-LAT data during the H.E.S.S. observations, so 95% C.L. upper limits are computed assuming an E^{-2} spectrum. We find differential energy flux upper limits (between 100 MeV and 10 GeV) of 7.1×10^{-10} and 2.6×10^{-10} erg cm⁻² s⁻¹ during Night 3 and Night 4, respectively; the upper limit for Night 3 is shown in Figure 4.

4. DISCUSSION

The H.E.S.S. upper limits, when combined with multi-wavelength observations, can be used to constrain possible emission scenarios of GRB 221009A several days after the prompt event. Figure 4 shows the spectral energy distribution (SED) including the results of the H.E.S.S., XRT, and LAT analyses. Also included are the optical *i*-band flux during the time of the H.E.S.S. observations (extracted from Figure 2 of Fulton et al. 2023) and a publicly available radio observation (Rhodes et al. 2022) that most closely matches the time window of the first night of H.E.S.S. observations.

The SEDs on all nights during which H.E.S.S. measurements took place are consistent with synchrotron emission from a single electron population. In such a model, the synchrotron spectrum peaks above the energy range covered by the XRT, implying Klein Nishina (KN) suppression of any inverse Compton (IC) component. For IC-dominated cooling, KN suppression could account for the hard cooled spectrum of electrons emitting in the XRT range (e.g. Agaronyan & Ambartsumyan 1985; Nakar et al. 2009; Breuhaus et al. 2021). However, this is difficult to reconcile with the H.E.S.S. upper limits in the VHE range, as electrons producing X-ray photons via synchrotron emission should produce a comparable or greater gamma-ray flux via their IC emission. The energy density of optical photons was insufficient for internal absorption of TeV photons, while the LHAASO detection suggests that absorption on a local external field was unlikely. Ruling out IC-dominated cooling, we consider instead models in which synchrotron dominated cooling can account for the multiwavelength observations. We adopt a single-zone thin shell model (see Huang et al. 2022b), assuming self-similar expansion of a relativistic shock following an impulsive point-like explosion (Blandford & McKee 1976).

Within this model, we assume the radio to X-ray emission is produced by single population of continuously injected electrons. The photon index of the XRT emission (see Table 2) was consistent with $\alpha \approx 1.8$ on all nights (see also Williams et al. 2023). Data from the Nuclear Spectroscopic Telescope Array (NuSTAR) indicate this spectrum continued unbroken above the XRT range (Laskar et al. 2023). These measurements imply either an uncooled electron population $dN_e/d\bar{\gamma}_e \propto \bar{\gamma}_e^{-2.6}$, or the cooled spectrum assuming continuous injection: $dN_{\text{inj}}/d\bar{\gamma}_e \propto \bar{\gamma}_e^{-1.6}$. Here $\bar{\gamma}_e$ is the electron Lorentz factor in the fluid frame. For the cooling break to remain above the NuSTAR range (3-79 keV), requires specific conditions (see for example Huang et al. 2022b, eq. 14). This scenario was considered by Laskar et al. (2023), who modelled the synchrotron component assuming a wind profile. To match the measured flux, more than half of the downstream internal energy needs to be converted to non-thermal electrons and magnetic field energy, with these two components being in near equipartition. The SSC flux is negligible in such a scenario. To maintain the cooling break above the X-ray range requires a low mass loss rate, and though low mass loss rates are expected from the polar regions of low-metallicity stars (Muijres et al. 2012), it is unclear if such a wind profile can be sustained over a large distance from the progenitor.

We consider the alternative possibility of a cooled hard injection spectrum, comparing against the first night of H.E.S.S. observations. To match the flux levels, we introduce a parameter $\eta_{\text{inj}} \leq 1$, the ratio of non-thermal particle density flux, to the particle density flux downstream. The injection energy is left as a free parameter, and since the total integrated energy for an injection spectrum with index < 2 is determined by the maximum electron energy, the is fixed by the energy efficiency. The model parameters provided in Table 3 were chosen to match the selected measurements, while just reaching the H.E.S.S. upper limits. The cooling break in the synchrotron component occurs between the radio and optical data points, at a flux level comparable to the H.E.S.S. upper limit. As synchrotron cooling dominates for the chosen parameters, the corresponding IC flux remains below the upper limits.

5. SUMMARY AND CONCLUSION

H.E.S.S. began observing GRB 221009A approximately 53 hours after the initial *Fermi*-GBM detection. The observations were taken under less-than-optimal atmospheric conditions caused by clouds and aerosols. No significant VHE signal is detected on the third, fourth, and ninth nights after the detection, nor in the combined dataset of all three nights. When

⁷ <https://fermi.gsfc.nasa.gov/ssc/data/access/lat/BackgroundModels.html>

Explosion energy E	10^{54} erg
External density n_{ext}	1.7 cm^{-3}
Injection fraction η_{inj}	0.1%
Electron equipartition fraction ϵ_e	9×10^{-4}
Magnetic equipartition fraction ϵ_B	8×10^{-4} (0.07G)

Table 3. Parameters used for single zone model fit, adopting the constant external-density solution of Blandford & McKee (1976). We choose $\bar{\gamma}_{\text{min}} = 0.66m_p/m_e$ where m_p/m_e the proton to electron mass ratio.

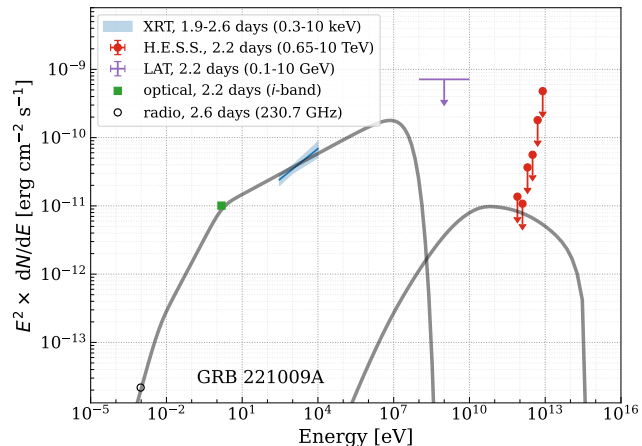


Figure 4. The H.E.S.S. 95% upper limits on Night 3 (red) are plotted along with the XRT (blue, 1σ) best-fit spectrum and LAT (purple, 95% C.L.) upper limit, as well as publicly available radio data from the Submillimeter Array (black open circle; Rhodes et al. (2022)) and an optical flux (green square; extracted from Figure 2 of Fulton et al. (2023)) in a multiwavelength SED. An example set of synchrotron and SSC emission components — arising from a single, partially cooled electron population described in Table 3 — are also shown to illustrate a possible explanation of the multiwavelength observations.

combining the data from all three nights, we find a 95% upper limit on the 0.65–10 TeV energy flux of $\Phi_{\text{UL}}^{95\%} = 9.7 \times 10^{-12} \text{ erg cm}^{-2} \text{ s}^{-1}$.

The H.E.S.S. upper limits help constrain possible emission scenarios when compared with the multiwavelength observations. The X-ray spectra on the three H.E.S.S. nights were found to remain hard, with photon indices ranging from 1.7 to 1.9. Taken together with the approximately contemporaneous optical and radio data, these measurements suggest synchrotron emission from a single electron population, with continuous injection of either an uncooled soft spectrum, or a cooled hard spectrum. The photon energy spectrum peaks above the XRT range, (and also that of the NuSTAR, Laskar et al. 2023) and KN suppression of any inverse Compton emission is unavoidable. An IC-dominated loss scenario

appears to be ruled out by the H.E.S.S. upper limits. In contrast, the multiwavelength SED of the nearby low-luminosity GRB 190829A, which was detected at TeV energies three nights after the prompt emission, was better described by a single component from X-rays to VHE gamma rays. Those data were consistent with photon indices ≈ 2 for both the XRT and H.E.S.S. energy ranges on all nights (Abdalla et al. (H.E.S.S. Collaboration) 2021). The results from GRB 221009A, potentially the brightest ever detected GRB, highlight the distinct character of these two bursts, both in terms of their non-thermal particle acceleration and emission properties. As discussed in Abdalla et al. (H.E.S.S. Collaboration) (2021) (see also Huang et al. 2022b; Salafia et al. 2022), an accurate reproduction of the MWL observations of GRB 190829A is challenging within a single-zone SSC framework. Other theoretical models put forward to account for the multiwavelength measurements of GRB 190829A, including external Compton (Zhang et al. 2021) or two-zone (Khangulyan et al. 2023) models serve to highlight the necessity for high quality spectral and temporal data of GRBs and their afterglows at all available wavelengths to understand the underlying physical mechanisms at play.

With upper-limits in the VHE band, we consider only a single-zone model for the first night of H.E.S.S. observations, assuming an electron population whose cooled spectrum is consistent with the inferred XRT spectrum. An alternative uncooled electron scenario was considered in Laskar et al. (2023) (see also Sato et al. 2022). The hard injection scenario requires a spectral index deviating substantially from that predicted from shock acceleration theory (e.g. Achterberg et al. 2001). Harder spectra have been predicted from other acceleration schemes such as relativistic shear acceleration (Rieger & Duffy 2005) or converter mechanisms (Derishev et al. 2003; Stern 2003; Derishev & Piran 2019). A detailed consideration of the underlying acceleration process is however beyond the scope of the current paper, though the emerging multiwavelength dataset for GRB 221009A will provide a valuable data set for future theoretical studies. Our results highlight the role imaging atmospheric Cherenkov telescopes have in improving our understanding of these powerful transient events.

ACKNOWLEDGMENTS

We thank Lauren Rhodes for discussions on the radio and optical data, and Phil Evans for assistance in analyzing XRT data. This work made use of data supplied by the UK Swift Science Data Centre at the University of Leicester.

The support of the Namibian authorities and of the University of Namibia in facilitating the construction and operation of H.E.S.S. is gratefully acknowledged, as is the support by the German Ministry for Education and Research (BMBF), the Max Planck Society, the German Research Foundation (DFG), the Helmholtz Association, the Alexander von Humboldt Foundation, the French Ministry of Higher Education, Research and Innovation, the Centre National de la Recherche Scientifique (CNRS/IN2P3 and CNRS/INSU), the Commissariat à l'énergie atomique et aux énergies alternatives (CEA), the U.K. Science and Technology Facilities Council (STFC), the Irish Research Council (IRC) and the Science Foundation Ireland (SFI), the Knut and Alice Wallenberg Foundation, the Polish Ministry of Education and Science, agreement no. 2021/WK/06, the South African Department of Science and Technology and National Research Foundation, the University of Namibia, the National Commission on Research, Science

& Technology of Namibia (NCRST), the Austrian Federal Ministry of Education, Science and Research and the Austrian Science Fund (FWF), the Australian Research Council (ARC), the Japan Society for the Promotion of Science, the University of Amsterdam and the Science Committee of Armenia grant 21AG-1C085. We appreciate the excellent work of the technical support staff in Berlin, Zeuthen, Heidelberg, Palaiseau, Paris, Saclay, Tübingen and in Namibia in the construction and operation of the equipment. This work benefited from services provided by the H.E.S.S. Virtual Organisation, supported by the national resource providers of the EGI Federation.

Software: Astropy (Astropy Collaboration et al. 2022), matplotlib (Hunter 2007), numpy (Harris et al. 2020), gammapy (Deil et al. 2017; Acero et al. 2022), XSPEC (Arnaud 1996), gtburst (Vianello 2016)

REFERENCES

- Abdalla et al. (H.E.S.S. Collaboration). 2019, *Nature*, 575, 464
- Abdalla et al. (H.E.S.S. Collaboration). 2021, *Science*, 372, 1081
- Abdollahi, S., Acero, F., Ackermann, M., et al. 2020, *ApJS*, 247, 33
- Acero, F., Aguasca-Cabot, A., Buchner, J., et al. 2022, if you use this software, please cite it using the metadata from this file.
- Achterberg, A., Gallant, Y. A., Kirk, J. G., & Guthmann, A. W. 2001, *MNRAS*, 328, 393
- Agaronyan, F. A. & Ambartsumyan, A. S. 1985, *Astrophysics*, 23, 650
- Aharonian et al. (H.E.S.S. collaboration). 2006, *A&A*, 457, 899
- Arnaud, K. A. 1996, in *Astronomical Society of the Pacific Conference Series*, Vol. 101, *Astronomical Data Analysis Software and Systems V*, ed. G. H. Jacoby & J. Barnes, 17
- Astropy Collaboration, Price-Whelan, A. M., Lim, P. L., et al. 2022, *ApJ*, 935, 167
- Atwood, W. B., Abdo, A. A., Ackermann, M., et al. 2009, *ApJ*, 697, 1071
- Berge, D., Funk, S., & Hinton, J. 2007, *A&A*, 466, 1219
- Bissaldi, E., Omodei, N., Kerr, M., & Fermi-LAT Team. 2022, *GRB Coordinates Network*, 32637, 1
- Blandford, R. D. & McKee, C. F. 1976, *Physics of Fluids*, 19, 1130
- Breuhaus, M., Hahn, J., Romoli, C., et al. 2021, *ApJL*, 908, L49
- Burrows, D. N., Hill, J. E., Nousek, J. A., et al. 2005, *SSRv*, 120, 165
- Campana, S., Lazzati, D., Perna, R., Grazia Bernardini, M., & Nava, L. 2021, *A&A*, 649, A135
- Dai, Z., Daigne, F., & Mészáros, P. 2017, *SSRv*, 212, 409
- de Jager, O. C., Harding, A. K., Michelson, P. F., et al. 1996, *ApJ*, 457, 253
- de Naurois, M. & Rolland, L. 2009, *Astroparticle Physics*, 32, 231
- de Ugarte Postigo, A., Izzo, L., Pugliese, G., et al. 2022, *GRB Coordinates Network*, 32648, 1
- Deil, C., Wood, M., Hassan, T., et al. 2022, *Data formats for gamma-ray astronomy - version 0.3*
- Deil, C., Zanin, R., Lefaucheur, J., et al. 2017, in *International Cosmic Ray Conference*, Vol. 301, 35th International Cosmic Ray Conference (ICRC2017), 766
- Derishev, E. & Piran, T. 2019, *ApJL*, 880, L27
- Derishev, E. V., Aharonian, F. A., Kocharovsky, V. V., & Kocharovsky, V. V. 2003, *PhRvD*, 68, 043003
- Dichiara, S., Gropp, J. D., Kennea, J. A., et al. 2022, *GRB Coordinates Network*, 32632, 1
- Domínguez, A., Primack, J. R., Rosario, D. J., et al. 2011, *MNRAS*, 410, 2556
- Evans, P. A. 2022, private communication
- Evans, P. A., Beardmore, A. P., Page, K. L., et al. 2009, *MNRAS*, 397, 1177

- Evans, P. A., Willingale, R., Osborne, J. P., et al. 2010, *A&A*, 519, A102
- Formenti, P., D'Anna, B., Flamant, C., et al. 2019, *Bulletin of the American Meteorological Society*, 100, 1277
- Fulton, M. D., Smartt, S. J., Rhodes, L., et al. 2023, The optical light curve of GRB 221009A: the afterglow and detection of the emerging supernova SN 2022xiw, <https://arxiv.org/abs/2301.11170>
- Hahn, J., de los Reyes, R., Bernlöhr, K., et al. 2014, *Astroparticle Physics*, 54, 25
- Harris, C. R., Millman, K. J., van der Walt, S. J., et al. 2020, *Nature*, 585, 357
- Holch, T. L., Leuschner, F., Schäfer, J., & Steinmassl, S. 2022, *Journal of Physics: Conference Series*, 2398, 012017
- Holler, M., Lenain, J. P., de Naurois, M., Rauth, R., & Sanchez, D. A. 2020, *Astroparticle Physics*, 123, 102491
- Holler, M. et al. 2015, *PoS, ICRC2015*, 847
- Huang, Y., Hu, S., Chen, S., et al. 2022a, *GRB Coordinates Network*, 32677, 1
- Huang, Z.-Q., Kirk, J. G., Giacinti, G., & Reville, B. 2022b, *ApJ*, 925, 182
- Hunter, J. D. 2007, *Computing in Science & Engineering*, 9, 90
- Iyyani, S. 2022, *Journal of Astrophysics and Astronomy*, 43, 37
- Khangulyan, D., Taylor, A. M., & Aharonian, F. 2023, *arXiv e-prints*, arXiv:2301.08578
- Laskar, T., Alexander, K. D., Margutti, R., et al. 2023, *arXiv e-prints*, arXiv:2302.04388
- Li, T.-P. & Ma, Y. 1983, *ApJ*, 272, 317
- MAGIC Collaboration, Acciari, V. A., Ansoldi, S., et al. 2019, *Nature*, 575, 455
- Mészáros, P. 2002, *ARA&A*, 40, 137
- Muijres, L., Vink, J. S., de Koter, A., et al. 2012, *A&A*, 546, A42
- Nakar, E., Ando, S., & Sari, R. 2009, *ApJ*, 703, 675
- Noda, K. & Parsons, R. D. 2022, *Galaxies*, 10, 7
- Ohm, S., van Eldik, C., & Egberts, K. 2009, *Astroparticle Physics*, 31, 383
- Parsons, R. D. & Hinton, J. A. 2014, *Astroparticle Physics*, 56, 26
- Planck Collaboration, Aghanim, N., Akrami, Y., et al. 2020, *A&A*, 641, A6
- Rhodes, L., Huang, K., & Cendes, Y. 2022, *GRB Coordinates Network*, 32707, 1
- Rieger, F. M. & Duffy, P. 2005, *ApJL*, 632, L21
- Rolke, W. A., López, A. M., & Conrad, J. 2005, *Nuclear Instruments and Methods in Physics Research A*, 551, 493
- Salafia, O. S., Ravasio, M. E., Yang, J., et al. 2022, *ApJL*, 931, L19
- Sato, Y., Murase, K., Ohira, Y., & Yamazaki, R. 2022, *arXiv e-prints*, arXiv:2212.09266
- Stern, B. E. 2003, *MNRAS*, 345, 590
- Tiengo, A., Pintore, F., Mereghetti, S., Salvaterra, R., & a larger Collaboration. 2022, *GRB Coordinates Network*, 32680, 1
- Tomankova, L., Yusafzai, A., Kostunin, D., et al. 2022, *Zenodo*, <https://doi.org/10.5281/zenodo.7400326>
- Veres, P., Burns, E., Bissaldi, E., et al. 2022, *GRB Coordinates Network*, 32636, 1
- Vianello, G. 2016, *gtburst: Release for Zenodo*
- Williams, M. A., Kennea, J. A., Dichiara, S., et al. 2023, *arXiv e-prints*, arXiv:2302.03642
- Willingale, R., Starling, R. L. C., Beardmore, A. P., Tanvir, N. R., & O'Brien, P. T. 2013, *MNRAS*, 431, 394
- Zhang, B. T., Murase, K., Veres, P., & Mészáros, P. 2021, *ApJ*, 920, 55

All Authors and Affiliations

F. AHARONIAN,^{1,2} F. AIT BENKHALI,³ J. ASCHERSLEBEN,⁴ H. ASHKAR,⁵ M. BACKES,^{6,7} A. BAKTASH,⁸
V. BARBOSA MARTINS,⁹ R. BATZOFIN,¹⁰ Y. BECHERINI,^{11,12} D. BERGE,^{9,13} K. BERNLÖHR,² B. BI,¹⁴
M. BÖTTCHER,⁷ C. BOISSON,¹⁵ J. BOLMONT,¹⁶ M. DE BONY DE LAVERGNE,¹⁷ J. BOROWSKA,¹³ M. BOUYAHIAOUI,²
F. BRADASCIO,¹⁸ M. BREUHAUS,² R. BROSE,¹ F. BRUN,¹⁸ B. BRUNO,¹⁹ T. BULIK,²⁰ C. BURGER-SCHIEDLIN,¹
S. CAROFF,¹⁷ S. CASANOVA,²¹ J. CELIC,¹⁹ M. CERRUTI,¹¹ T. CHAND,⁷ S. CHANDRA,⁷ A. CHEN,²²
J. CHIBUEZE,⁷ O. CHIBUEZE,⁷ G. COTTER,²³ S. DAI,²⁴ J. DAMASCENE MBARUBUCYEYE,⁹ J. DEVIN,²⁵
A. DJANNATI-ATAÏ,¹¹ A. DMYTRIIEV,⁷ V. DOROSHENKO,¹⁴ K. EGBERTS,¹⁰ S. EINECKE,²⁶ J.-P. ERNENWEIN,²⁷
S. FEGAN,⁵ G. FICHET DE CLAIRFONTAINE,¹⁵ M. FILIPOVIC,²⁴ G. FONTAINE,⁵ M. FÜSSLING,⁹ S. FUNK,¹⁹
S. GABICI,¹¹ S. GHAFOURIZADEH,³ G. GIAVITTO,⁹ D. GLAWION,¹⁹ J.F. GLICENSTEIN,¹⁸ P. GOSWAMI,⁷
G. GROLLERON,¹⁶ M.-H. GRONDIN,²⁸ J.A. HINTON,² T. L. HOLCH,⁹ M. HOLLER,²⁹ D. HORNS,⁸ ZHIQIU HUANG,²
M. JAMROZY,³⁰ F. JANKOWSKY,³ V. JOSHI,¹⁹ I. JUNG-RICHARDT,¹⁹ E. KASAI,⁶ K. KATARZYŃSKI,³¹
R. KHATOON,⁷ B. KHÉLIFI,¹¹ W. KLUŻŃIAK,³² NU. KOMIN,²² R. KONNO,⁹ K. KOSACK,¹⁸ D. KOSTUNIN,⁹
R.G. LANG,¹⁹ S. LE STUM,²⁷ F. LEITL,¹⁹ A. LEMIERE,¹¹ M. LEMOINE-GOUMARD,²⁸ J.-P. LENAIN,¹⁶
F. LEUSCHNER,¹⁴ T. LOHSE,¹³ I. LYPOVA,³ J. MACKEY,¹ D. MALYSHEV,¹⁴ D. MALYSHEV,¹⁹ V. MARANDON,²
P. MARCHEGANI,²² A. MARCOWITH,²⁵ G. MARTÍ-DEVESA,²⁹ R. MARX,³ M. MEYER,⁸ A. MITCHELL,¹⁹
L. MOHRMANN,² A. MONTANARI,³ E. MOULIN,¹⁸ T. MURACH,⁹ K. NAKASHIMA,¹⁹ M. DE NAUROIS,⁵ J. NIEMIEC,²¹
A. PRIYANA NOEL,³⁰ P. O'BRIEN,³³ S. OHM,⁹ L. OLIVERA-NIETO,² E. DE ONA WILHELMI,⁹ M. OSTROWSKI,³⁰
S. PANNY,²⁹ M. PANTER,² R.D. PARSONS,¹³ G. PERON,¹¹ D.A. PROKHOROV,³⁴ H. PROKOPH,⁹ G. PÜHLHOFER,¹⁴
M. PUNCH,¹¹ A. QUIRRENBACH,³ P. REICHHERZER,¹⁸ A. REIMER,²⁹ O. REIMER,²⁹ H. REN,² M. RENAUD,²⁵
B. REVILLE,² F. RIEGER,² G. ROWELL,²⁶ B. RUDAK,³² E. RUIZ-VELASCO,² V. SAHAKIAN,³⁵ H. SALZMANN,¹⁴
A. SANTANGELO,¹⁴ M. SASAKI,¹⁹ J. SCHÄFER,¹⁹ F. SCHÜSSLER,¹⁸ H.M. SCHUTTE,⁷ U. SCHWANKE,¹³
J.N.S. SHAPOPI,⁶ A. SPECOVIVUS,¹⁹ S. SPENCER,¹⁹ L. STAWARZ,³⁰ R. STEENKAMP,⁶ S. STEINMASSL,² C. STEPPA,¹⁰
I. SUSHCH,⁷ H. SUZUKI,³⁶ T. TAKAHASHI,³⁷ T. TANAKA,³⁶ R. TERRIER,¹¹ N. TSUJI,³⁸ Y. UCHIYAMA,³⁹
M. VECCHI,⁴ C. VENTER,⁷ J. VINK,³⁴ S.J. WAGNER,³ R. WHITE,² A. WIERZCHOLSKA,²¹ YU WUN WONG,¹⁹
M. ZACHARIAS,^{3,7} D. ZARGARYAN,¹ A.A. ZDZIARSKI,³² A. ZECH,¹⁵ S.J. ZHU⁹ AND N. ŻYWUCKA⁷

H.E.S.S. COLLABORATION

¹Dublin Institute for Advanced Studies, 31 Fitzwilliam Place, Dublin 2, Ireland

²Max-Planck-Institut für Kernphysik, P.O. Box 103980, D 69029 Heidelberg, Germany

³Landessternwarte, Universität Heidelberg, Königstuhl, D 69117 Heidelberg, Germany

⁴Kapteyn Astronomical Institute, University of Groningen, Landleven 12, 9747 AD Groningen, The Netherlands

⁵Laboratoire Leprince-Ringuet, École Polytechnique, CNRS, Institut Polytechnique de Paris, F-91128 Palaiseau, France

⁶University of Namibia, Department of Physics, Private Bag 13301, Windhoek 10005, Namibia

⁷Centre for Space Research, North-West University, Potchefstroom 2520, South Africa

⁸Universität Hamburg, Institut für Experimentalphysik, Luruper Chaussee 149, D 22761 Hamburg, Germany

⁹DESY, D-15738 Zeuthen, Germany

¹⁰Institut für Physik und Astronomie, Universität Potsdam, Karl-Liebknecht-Strasse 24/25, D 14476 Potsdam, Germany

¹¹Université de Paris, CNRS, Astroparticule et Cosmologie, F-75013 Paris, France

¹²Department of Physics and Electrical Engineering, Linnaeus University, 351 95 Växjö, Sweden

¹³Institut für Physik, Humboldt-Universität zu Berlin, Newtonstr. 15, D 12489 Berlin, Germany

¹⁴Institut für Astronomie und Astrophysik, Universität Tübingen, Sand 1, D 72076 Tübingen, Germany

¹⁵Laboratoire Univers et Théories, Observatoire de Paris, Université PSL, CNRS, Université de Paris, 92190 Meudon, France

¹⁶Sorbonne Université, Université Paris Diderot, Sorbonne Paris Cité, CNRS/IN2P3, Laboratoire de Physique Nucléaire et de Hautes Energies, LPNHE, 4 Place Jussieu, F-75252 Paris, France

¹⁷Université Savoie Mont Blanc, CNRS, Laboratoire d'Annecy de Physique des Particules - IN2P3, 74000 Annecy, France

¹⁸IRFU, CEA, Université Paris-Saclay, F-91191 Gif-sur-Yvette, France

¹⁹Friedrich-Alexander-Universität Erlangen-Nürnberg, Erlangen Centre for Astroparticle Physics, Erwin-Rommel-Str. 1, D 91058 Erlangen, Germany

²⁰Astronomical Observatory, The University of Warsaw, Al. Ujazdowskie 4, 00-478 Warsaw, Poland

²¹Instytut Fizyki Jądrowej PAN, ul. Radzikowskiego 152, 31-342 Kraków, Poland

²²School of Physics, University of the Witwatersrand, 1 Jan Smuts Avenue, Braamfontein, Johannesburg, 2050 South Africa

²³University of Oxford, Department of Physics, Denys Wilkinson Building, Keble Road, Oxford OX1 3RH, UK

²⁴School of Science, Western Sydney University, Locked Bag 1797, Penrith South DC, NSW 2751, Australia

²⁵Laboratoire Univers et Particules de Montpellier, Université Montpellier, CNRS/IN2P3, CC 72, Place Eugène Bataillon, F-34095 Montpellier Cedex 5, France

²⁶School of Physical Sciences, University of Adelaide, Adelaide 5005, Australia

²⁷ Aix Marseille Université, CNRS/IN2P3, CPPM, Marseille, France

²⁸ Université Bordeaux, CNRS, LP2I Bordeaux, UMR 5797, F-33170 Gradignan, France

²⁹ Leopold-Franzens-Universität Innsbruck, Institut für Astro- und Teilchenphysik, A-6020 Innsbruck, Austria

³⁰ Obserwatorium Astronomiczne, Uniwersytet Jagielloński, ul. Orła 171, 30-244 Kraków, Poland

³¹ Institute of Astronomy, Faculty of Physics, Astronomy and Informatics, Nicolaus Copernicus University, Grudziadzka 5, 87-100 Torun, Poland

³² Nicolaus Copernicus Astronomical Center, Polish Academy of Sciences, ul. Bartycka 18, 00-716 Warsaw, Poland

³³ Department of Physics and Astronomy, The University of Leicester, University Road, Leicester, LE1 7RH, United Kingdom

³⁴ GRAPPA, Anton Pannekoek Institute for Astronomy, University of Amsterdam, Science Park 904, 1098 XH Amsterdam, The Netherlands

³⁵ Yerevan Physics Institute, 2 Alikhanian Brothers St., 375036 Yerevan, Armenia

³⁶ Department of Physics, Konan University, 8-9-1 Okamoto, Higashinada, Kobe, Hyogo 658-8501, Japan

³⁷ Kavli Institute for the Physics and Mathematics of the Universe (WPI), The University of Tokyo Institutes for Advanced Study (UTIAS), The University of Tokyo, 5-1-5 Kashiwa-no-Ha, Kashiwa, Chiba, 277-8583, Japan

³⁸ RIKEN, 2-1 Hirosawa, Wako, Saitama 351-0198, Japan

³⁹ Department of Physics, Rikkyo University, 3-34-1 Nishi-Ikebukuro, Toshima-ku, Tokyo 171-8501, Japan